Geometric origin of self-intersection points in non-Hermitian energy spectra

Jinghui Pi [1,*,†] Chenyang Wang [2,*] Yong-Chun Liu [2,3] and Yangqian Yan [4,1,‡]

[1]*The Chinese University of Hong Kong Shenzhen Research Institute, 518057 Shenzhen, China*
[2]*State Key Laboratory of Low-Dimensional Quantum Physics, Department of Physics, Tsinghua University, Beijing 100084, China*
[3]*Frontier Science Center for Quantum Information, Beijing 100084, China*
[4]*Department of Physics, The Chinese University of Hong Kong, Shatin, New Territories, Hong Kong, China*

Unlike Hermitian systems, non-Hermitian energy spectra under periodic boundary conditions can form closed loops in the complex energy plane, a phenomenon known as the point-gap topology. In this paper, we investigate the self-intersection points of such non-Hermitian energy spectra and reveal their geometric origins. We rigorously demonstrate that these self-intersection points result from the intersection of the auxiliary generalized Brillouin zone and the Brillouin zone in one-band systems, as confirmed by an extended Hatano-Nelson model. This finding is further generalized to multiband systems, illustrated through a non-Hermitian Su-Schrieffer-Heeger model. Moreover, we address multiple self-intersection points and derive the geometric conditions for general n-fold self-intersection points. Our results enhance the fundamental understanding of generic non-Hermitian quantum systems and provide theoretical support for further experimental investigations of energy self-intersection points.

I. INTRODUCTION

Non-Hermiticity emerges when a closed system couples with its environment [1]. It has been realized in many experimental platforms, including optical systems with gain and loss [2–4], open systems with dissipation [5], and electron systems with finite-lifetime quasiparticles [6–8]. A variety of phenomena beyond traditional paradigms have been revealed [9–16], including the non-Hermitian skin effect (NHSE) [17–22], which refers to the boundary localization of a large portion of eigenstates. The NHSE renders a high sensitivity of spectra to the boundary conditions, thereby breaking conventional bulk-edge correspondence [23–25]. A central concept related to the NHSE is the generalized Brillouin zone (GBZ) [18,19]. By replacing the Brillouin zone (BZ) with the GBZ, one can establish the non-Bloch-band theory and reshape the bulk-edge correspondence [26–38]. An efficient analytical and numerical approach to obtaining the GBZ is the auxiliary GBZ (aGBZ) method [39,40], which also manifests the critical NHSE [41–44].

The topological origin of the NHSE is the nontrivial non-Hermitian point gap [29,45–48]. Specifically, the energy spectra under periodic boundary conditions (PBC) form a closed loop enclosing a finite area when systems feature the NHSE under the open boundary conditions (OBC). Such PBC energy spectra can be categorized into two types: simple closed curves with a single connected interior region, and self-intersecting closed curves that partition the interior into distinct subregions. When systems exhibit the bipolar skin effect [49,50], the PBC energy spectra must have self-intersection points and belong to the latter type of curves. However, if all skin modes are localized at one boundary, the PBC energy spectra may also display self-intersection points [51]. Therefore, it remains unclear how these self-intersection points arise in the PBC energy spectra.

In this work, we examine self-intersection points within general one-dimensional (1D) non-Hermitian energy spectra and offer a comprehensive explanation for the geometric origins of these points. Notably, as non-Hermitian degeneracies, energy self-intersection points are distinct from exceptional points [5,52–58], where eigenstates are coalesced. For convenience, we review the one-band theory in one-dimensional non-Hermitian systems and introduce the concept of the energy winding number, the GBZ, and the aGBZ. We uncover that, for one-band systems, the PBC energy spectra exhibit self-intersection points if and only if the corresponding aGBZ curve intersects with the unit circle (the BZ curve), and vice versa. This finding is rigorously demonstrated through a topological method and confirmed by numerical investigations of an extended Hatano-Nelson model. Furthermore, we extend our analysis to the multiband cases and illustrate the results through a non-Hermitian Su-Schrieffer-Heeger (SSH) model. Additionally, we discuss the multiple self-intersection points with multiplicities greater than two, deriving the geometric conditions for general n-fold self-intersection points. Our findings advance the foundational understanding of the spectra of generic non-Hermitian quantum systems, and offer theoretical justification for further experimental explorations of energy self-intersection points.

The rest of the paper is organized as follows. We provide a brief review of the fundamental concept of the one-band non-Hermitian systems in Sec. II, including the energy winding number, the GBZ, and the aGBZ. In Sec. III, we rigor-

---

*These authors contributed equally to this work.

†Contact author: pijh14@gmail.com

‡Contact author: yqyan@cuhk.edu.hk

ously prove that self-intersecting points in one-band PBC energy spectra originate from the intersection of the aGBZ and the BZ. The above one-band conclusion is extended to the multiband cases in Sec. IV, and the geometric conditions for general n-fold self-intersection points is established in Sec. V. Finally, a summary and discussion are presented in Sec. VI.

II. REVIEW OF ONE-BAND NON-HERMITIAN SYSTEMS

We begin with a general one-band tight-binding model in one dimension. The real-space Hamiltonian reads

$$H = \sum_{i,j} t_{j-i} |i\rangle\langle j|, \tag{1}$$

where i, j are the position indices and the hopping amplitudes, t_{j-i}, depend solely on the spatial distance $j - i$ and have finite range with left (right) hopping range M (N). Applying the Fourier transformation of hopping amplitudes, we obtain the Bloch Hamiltonian,

$$h(k) = \sum_{n=-M}^{N} t_n (e^{ik})^n. \tag{2}$$

For the periodic boundary condition, the Bloch phase factor e^{ik} moves along the unit circle on the complex plane with $0 \leqslant k < 2\pi$,. In the Hermitian case, where $t_n = t_{-n}^*$, the spectrum of $h(k)$ lies on the real axis and thus encloses zero area. However, for the non-Hermitian systems with $t_n \neq t_{-n}^*$, the spectrum of $h(k)$ can form a closed curve in the complex energy plane and encloses a finite area. Such a distinct topological behavior is characterized by the winding number $W(E_b) \in \mathbb{Z}$, defined as [45,46]:

$$W(E_b) = \int_0^{2\pi} \frac{dk}{2\pi i} \partial_k \ln(h(k) - E_b), \tag{3}$$

where $E_b \in \mathbb{C}$ is a reference point. If $W(E_b) \neq 0$ for some E_b, the system under the OBC features the non-Hermitian skin effect, which is a consequence of nontrivial point-gap topology [29,46].

To obtain the OBC energy spectrum and quantify the non-Hermitian skin modes, we take the analytic continuation of $h(k)$ by making the substitution $e^{ik} \rightarrow \beta = e^{\mu+ik}$ (k and μ are real valued). Then, for each $h(k)$, there exists a holomorphic function

$$h(\beta) = t_{-M}\beta^{-M} + \cdots t_N\beta^N = \frac{P_{M+N}(\beta)}{\beta^M}, \tag{4}$$

where $P_{M+N}(\beta)$ is a polynomial of order $M + N$. According to the fundamental theorem of algebra, for any $E \in \mathbb{C}$, the characteristic equation $f(\beta, E) = h(\beta) - E = 0$ has $M + N$ roots of β. We can order these roots in ascending amplitude $|\beta_1(E)| \leqslant |\beta_2(E)| \leqslant \cdots \leqslant |\beta_{M+N}(E)|$, and the GBZ is determined by the following equation [18,26,29]:

$$|\beta_M(E)| = |\beta_{M+1}(E)|. \tag{5}$$

All solutions of β_M, β_{M+1} trace a closed curve, termed the GBZ, in complex β plane. This curve encapsulates critical information about eigenstate profiles, including the conventional wave vector k and the spatial decay rate μ of a skin

mode. Upon obtaining the GBZ, we can acquire the OBC energy spectrum in the thermodynamic (large-size) limit by inserting $\beta \in$ GBZ into Eq. (4). Furthermore, replacing the BZ with the GBZ allows us to define the topological invariants that dictate the topological boundary modes, thereby establishing the non-Bloch bulk-edge correspondence. Consequently, the GBZ serves a role analogous to the BZ in Hermitian systems and occupies a central position in the non-Bloch band theory.

A concept closely related to the GBZ is the aGBZ [40], defined by projecting the following two equations onto the complex β plane,

$$f(\beta, E) = f(\beta e^{i\theta}, E) = 0, \theta \in \mathbb{R}. \tag{6}$$

Since there are five variables ($\text{Im}\,\beta$, $\text{Re}\,\beta$, $\text{Re}\,E$, $\text{Im}\,E$, θ) and four constraint equations $\text{Re}\,f = \text{Im}\,f = \text{Re}\,f_\theta = \text{Im}\,f_\theta = 0$, where $f_\theta = f(\beta e^{i\theta}, E)$, the solution of Eq. (6) forms a 1D curve in the 5D space. The analytical expression of aGBZ can be calculated via the resultant method to eliminate the additional variables θ and E. The resulting equation is an algebraic equation of $\text{Re}\,\beta$ and $\text{Im}\,\beta$, given by

$$\sum_{ij} c_{ij} (\text{Re}\,\beta)^i (\text{Im}\,\beta)^j = 0. \tag{7}$$

The aGBZ described by Eq. (7) is a complicated curve in complex β plane, composed of a set of analytic arcs connected at the self-intersection points. Specifically, each analytic arc consists of conjugate pair (β_0, $\tilde{\beta}_0$), where $\tilde{\beta}_0 = \beta_0 e^{i\theta_0}$, satisfying $f(\beta_0, E_0) = f(\tilde{\beta}_0, E_0) = 0$. Then, solving $f(\beta, E_0) = 0$ and ordering the roots by the absolute value, we can identify the ordering of two roots that have the same absolute value as $|\beta_0|$. For example, if $|\beta_0| = |\beta_M(E_0)| = |\beta_{M+1}(E_0)|$, the ordering of β_0 is $(M, M + 1)$, which helps us pick up the GBZ from the aGBZ. Any points in an analytic arc have the same root ordering, changing only at the self-intersection points.

III. SELF-INTERSECTION IN ONE-BAND NON-HERMITIAN ENERGY SPECTRUM

For one-band energy spectra with nontrivial point-gap topology, the band structure can be categorized into two types: simple closed curves enclosing a single connected region or self-intersecting closed curves partitioning the interior into distinct subregions. To analyze the self-intersection points in the latter type of energy spectra, we define the following winding number

$$w(\mathcal{C}, E_b) = \oint_{\mathcal{C}} \frac{d\beta}{2\pi i} \partial_\beta \ln[h(\beta) - E_b], \tag{8}$$

where $\mathcal{C}$ is a closed contour in complex β plane. Especially, if $\mathcal{C}$ is the unit circle (the BZ), then Eq. (8) reduces to Eq. (3). According to the argument principle, the winding number of a complex function is the difference between the total number of zeros and poles enclosed by $\mathcal{C}$ [59], namely

$$w(\mathcal{C}, E_b) = N_1 - N_2, \tag{9}$$

where $N_1(N_2)$ is the count of zeros (poles) with their respective multiplicities. As the contour $\mathcal{C}$ encloses the origin, we always have $N_2 = M$. Therefore, the winding number
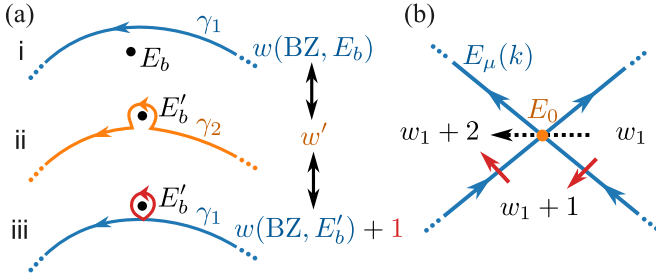
FIG. 1. Relations of the winding numbers in distinct subregions. (a) Change of the winding number when the reference point passes across the PBC energy spectrum. E_b and E_b' denote two different reference points, and the colored curves denote the loops in the complex energy plane. Panels i–iii show three equivalent loops with the same total winding number. (b) Winding numbers in the neighborhood of a self-intersection point. The blue lines denote the PBC spectrum, the orange point is the self-intersection point. The blue arrows denote the direction of k, and the winding number in the four subregions are marked in the figure.

$w(\mathcal{C}, E_b)$ is determined by the number of zeros of $P_{M+N}(\beta) - \beta^M E_b$ that lie within the contour $\mathcal{C}$.

Since the winding number defined in Eq. (3) is a topological number, it only changes when E_b passes across the PBC spectrum, and the increment or decrement of the winding number is determined by the direction in which E_b crosses the PBC spectrum. As illustrated in Fig. 1(a), consider a reference point moving across a segment of the PBC spectrum [curve γ_1 in Fig. 1(a)] from the left-hand side (E_b) to the right-hand side (E_b'), viewed from the direction in which k increases. To calculate $w(\mathrm{BZ}, E_b) - w(\mathrm{BZ}, E_b')$, we continuously change the loop γ_1 into an auxiliary loop γ_2, shown as the panel ii in Fig. 1(a). From i to ii, the reference point does not pass the loop, so that the winding number of the loop γ_2 around E_b', denoted as w', equals $w(\mathrm{BZ}, E_b)$. Based on the auxiliary loop, we close the detour into a small loop (red loop in panel iii), and recover the PBC spectrum, then the winding number w' equals the sum of the two loops, i.e., $w(\mathrm{BZ}, E_b) = w' = w(\mathrm{BZ}, E_b') + 1$. As a result, when the reference point crosses the PBC spectrum from the left to the right, the spectral winding number decreases by 1, and vice versa.

When the PBC spectrum is a self-intersecting closed curve, its interior is divided into distinct subregions, which is connected by the self-intersection points. As illustrated in Fig. 1(b), we consider the simple crossing of the PBC spectrum at one intersection point E_0. The direction of k is marked by the blue arrows. The crossing at the intersection point can be viewed as a node with four directed edges in graph theory. Because the PBC spectrum is closed loop on the complex plane, the number of edges towards the intersection point must equal the number of edges directed from the intersection point. Therefore, it is always possible for a reference point to cross the PBC spectrum twice from the right to the left, as illustrated by the red arrows in Fig. 1(b). Supposing the winding number around the start point is w_1, because each crossing will increase the winding number by 1, so that the winding number around the end point equals $w_1 + 2$. In the following, we demonstrate that such a self-intersection point E_0 corresponds to the intersection points of the BZ curve and

the aGBZ curve in the complex β plane. We first show that the self-intersection point E_0 corresponds to the points on the unit circle of the complex β plane. Since E_0 belongs to the PBC spectrum, the characteristic equation $f(\beta, E_0) = 0$ must have two different solutions $\beta_0^{(1)}(E_0) = e^{ik_1}$, $\beta_0^{(2)}(E_0) = e^{ik_2}$, where $k_1, k_2 \in (0, 2\pi]$. Consequently, both $\beta_0^{(1)}$ and $\beta_0^{(2)}$ reside on the unit circle of complex β plane (namely the BZ curve).

Then, we show that $\beta_0^{(1)}$ and $\beta_0^{(2)}$ also lie on the aGBZ curve. In fact, the aGBZ curve can be regarded as all possible solutions of $f(\beta, E) = 0$ satisfying $|\beta_i(E)| = |\beta_j(E)|$ for any $i \neq j$. Specifically, we define a set of curves $\partial\mathcal{B}_{i,i+1} = \{\beta \in \mathbb{C} | \forall E \in \mathbb{C} : |\beta_i(E)| = |\beta_{i+1}(E)|\}(1 \leqslant i \leqslant M + N - 1)$, where the roots of $f(\beta, E) = 0$ are ordered by their magnitude $|\beta_1(E)| \leqslant \cdots \leqslant |\beta_{m+n}(E)|$. The aGBZ is the union of all these curves, that is, aGBZ $= \partial\mathcal{B}_{1,2} \cup \cdots \cup \partial\mathcal{B}_{M+N-1,M+N}$, and the GBZ is just $\partial\mathcal{B}_{M,M+1}$. Each curve $\partial\mathcal{B}_{i,i+1}$ forms a closed loop, enclosing i zeros of the equation $f(\beta, E) = 0$ for arbitrary E (see details in Appendix B). On the other hand, the interior of the self-intersected PBC spectrum is partitioned into several subregions. Consider two subregions, labeled I and II, connected by the self-intersection point E_0. For any reference point E_{b1} in subregion I, the winding number along the BZ is

$$w(\mathrm{BZ}, E_{b1}) = l_1 - M \equiv w_1, \tag{10}$$

where l_1 is the number of zeros within the unit circle for the characteristic equation $f(\beta, E_{b1}) = 0$. Similarly, for any reference point E_{b2} in subregion II, we have

$$w(\mathrm{BZ}, E_{b2}) = l_2 - M \equiv w_2, \tag{11}$$

where l_2 is the number of zeros within the unit circle for $f(\beta, E_{b2}) = 0$. Note that $l_1(l_2)$ remains invariant for any $E_{b1}(E_{b2})$ within subregion I (II). As illustrated in Fig. 1(b), there always exist two different regions around the self-intersection points that satisfy $l_2 = l_1 + 2$ (i.e., $w_2 = w_1 + 2$). The reference points E_{b1} and E_{b2} can be connected through a path $\mathcal{S}$ that passes through E_0, with the remaining points of $\mathcal{S}$ belonging to subregions I and II. As E_{b1} moves towards E_0 along the path $\mathcal{S}$, the distances between E_{b1} and E_0 can become arbitrarily small, while there remain l zeros within the BZ curve. Once this reference point traverses E_0 and enters subregion II, the number of zeros within the unit circle increases by two, resulting in $l_1 + 2$. Therefore, the corresponding solutions for $f(\beta, E_0) = 0$, $\beta_0^{(1)}(E_0)$ and $\beta_0^{(2)}(E_0)$, are the boundary points separating the regions with l_1 and $l_1 + 2$ zeros within the BZ curve, and thus belong to $\partial\mathcal{B}_{l_1+1,l_1+2}$. As a result, $\beta_0^{(1)}(E_0)$ and $\beta_0^{(2)}(E_0)$ are the intersection points of the BZ and the aGBZ subcurve $\partial\mathcal{B}_{l_1+1,l_1+2}$.

On the other hand, if the aGBZ intersects with the BZ, e.g., a point of the aGBZ β such that $|\beta(E)| = 1$, the definition of the aGBZ implies the existence of at least one distinct point β' that also satisfies $|\beta'(E)| = 1$. Hence, we can express $\beta(E) = e^{ik}$ and $\beta'(E) = e^{ik'}$ with $k \neq k'$. This indicates that E is a self-intersection point of the PBC energy spectrum.

To illustrate the above results, we consider an extended Hatano-Nelson model with next-nearest-neighbor hopping [60,61], shown in Fig. 2(a). The generalized Bloch Hamiltonian is given by

$$h_{\mathrm{HN}}(\beta) = t_{-2}\beta^{-2} + t_{-1}\beta^{-1} + t_1\beta + t_2\beta^2. \tag{12}$$
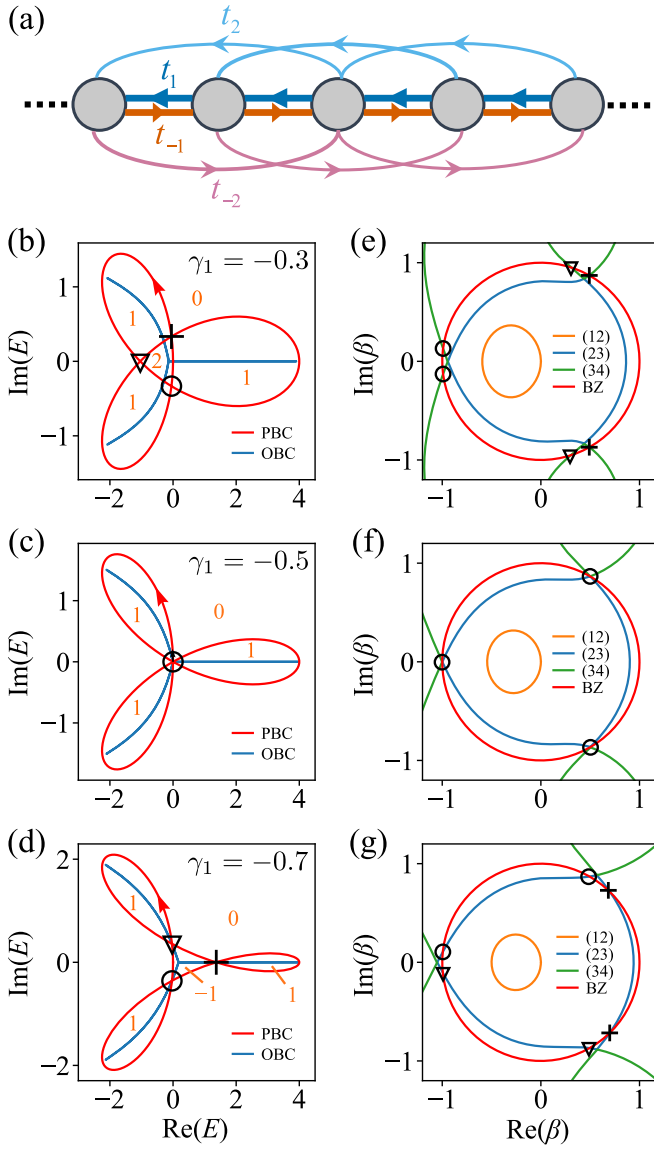
FIG. 2. (a) Schematic of an extended Hatano-Nelson model with next-nearest-neighbor hopping. (b)–(d) display the PBC (red line) and OBC (blue line) spectra of the model with varied parameters $t_1 = 1 + \gamma_1$ and $t_{-1} = 1 - \gamma_1$, where self-intersection points of the PBC energy spectra are marked by different shapes. Integer numbers in various regions denote winding numbers of the PBC energy spectra. (e)–(g) The corresponding aGBZs. Different colors represent different root orderings of the analytic arcs $|\beta_i(E)| = |\beta_{i+1}(E)|$. Solutions for self-intersection points in complex β plane are marked with the relevant shapes, denoting intersections between the aGBZ and the BZ. Throughout (b)–(g), we set $t_2 = 1.5$ and $t_{-2} = 0.5$.

If all hopping parameters are real, the real-space Hamiltonian H_{HN} obeys the generalized PT symmetry $\mathcal{K} H_{\text{HN}} \mathcal{K} = H_{\text{HN}}$, where $\mathcal{K}$ is the complex conjugate operator [62,63]. The characteristic equation $h_{\text{HN}}(\beta) - E = 0$ has two poles and four zeros in complex β plane. Therefore, the winding number $w(\mathcal{C}, E_b)$ for $h_{\text{HN}}(\beta)$ along the curve $\mathcal{C} = \text{BZ}$ can take integer values ranging from -2 to 2. Furthermore, a self-intersection point of the PBC energy spectrum correspond to two solutions of β located on the unite circle. When $t_{-2} = t_2 = 0$, this model

reduces to the standard Hatano-Nelson model and the aGBZ is a circle with radius $\sqrt{|t_1/t_{-1}|}$ in the complex β plane. For nonzero t_{-2} and t_2, the aGBZ deviates from a circle and can be obtained analytically using the resultant method detailed in Appendix A.

We present the energy spectra in Figs. 2(b)–2(d) and their corresponding aGBZs in Figs. 2(e)–2(g), with $t_2 = 1.5$ and $t_{-2} = 0.5$ fixed. The other two parameters are set as $t_1 = 1 + \gamma_1$ and $t_{-1} = 1 - \gamma_1$. When $\gamma_1 = -0.3$, the interior of the PBC spectrum is divided into four distinct subregions: three with a winding number of 1 and one with a winding number of 2 [see Fig. 2(b)]. In this scenario, the self-intersection points correspond to solutions of the characteristic equation satisfying $|\beta_3(E)| = |\beta_4(E)| = 1$, which represent the intersection points between the GBZ and the unit circle, as shown in Fig. 2(e). For $\gamma_1 = -0.7$, the interior of the PBC spectrum is similarly divided into four distinct subregions, three with a winding number of 1 and one with a winding number of -1 [see Fig. 2(d)]. The self-intersection points of the PBC spectrum, in this case, correspond to solutions of the characteristic equation satisfying $|\beta_2(E)| = |\beta_3(E)| = 1$, as illustrated in Fig. 2(g). At $\gamma_1 = -0.5$, all self-intersection points are merged at zero energy, leading to three subregions, all with a winding number of 1 [see Fig. 2(c)]. In this scenario, the self-intersection points satisfy the condition $|\beta_2(E)| = |\beta_3(E)| = |\beta_4(E)| = 1$, as shown in Fig. 2(f). To analyze this condition, we consider $\gamma_1 = -0.5 + \epsilon$, where ϵ is a small perturbation. For a negative infinitesimal value of ϵ, there exists a infinite small loop with a winding number of -1, admitting $|\beta_2(E)| = |\beta_3(E)| = 1$ at the self-intersection points. Conversely, for a positive infinitesimal ϵ, a infinite small loop with a winding number of 2 emerges, resulting in $|\beta_3(E)| = |\beta_4(E)| = 1$ at these points. Therefore, this triple self-intersection point corresponds to $|\beta_2(E)| = |\beta_3(E)| = |\beta_4(E)| = 1$ in complex β plane. Interestingly, the OBC spectra in Figs. 2(b)–2(d) exhibit non-Bloch PT symmetry breaking [27,64–66], where exceptional points arise. This type of non-Hermitian degeneracy corresponds to cusps of the GBZ curve in Figs. 2(e)–2(g) [67].

IV. SELF-INTERSECTION POINTS IN MULTI-BAND NON-HERMITIAN ENERGY SPECTRUM

For a one-dimensional multiband Hamiltonian, the characteristic equation is now given by

$$f(\beta, E) = \det[h(\beta) - E] = 0. \tag{13}$$

This equation defines a two-dimensional Riemann surface in the four-dimensional space (Re β, Im β, Re E, Im E). As $f(\beta, E) = \prod_{\mu=1}^{n}[E - E_\mu(\beta)] = 0$, each band $E = E_\mu(\beta)$ corresponds to a branch of the multivalued function. Similar to the one-band case, the aGBZ is determined by the two roots of Eq. (13) with identical amplitudes. However, self-intersection points in multiband cases can come from intersections between curves within the same sub-band or across different sub-bands. Therefore, the winding number should include the contributions from all sub-bands, namely

$$w(\mathcal{C}, E_b) = \oint_{\mathcal{C}} \frac{d\beta}{2\pi i} \partial_\beta \ln \det[h(\beta) - E_b], \tag{14}$$
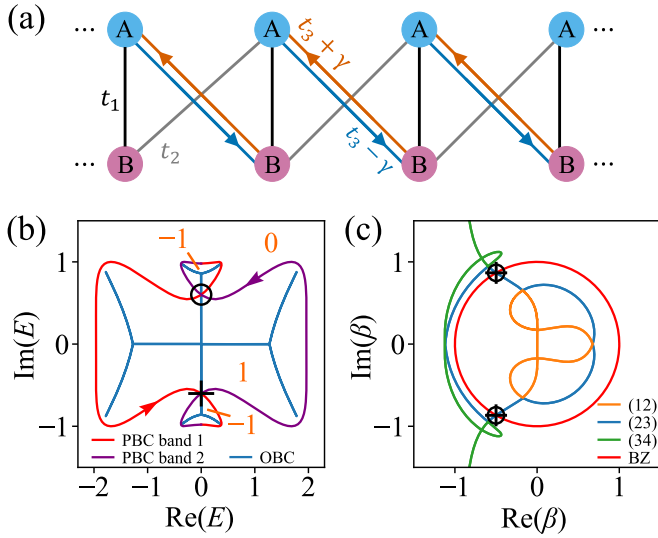
FIG. 3. (a) The schematic of a non-Hermitian SSH model. (b) The PBC and OBC spectra in the complex energy plane. The self-intersection points of PBC energy spectra occur between two bands and are marked by different shapes. (c) The corresponding aGBZ in complex β plane. Due to the chiral symmetry, the solutions for β at self-intersection points are twofold degenerate and denote the intersection of the aGBZ and the BZ. In (b) and (c), we set $t_1 = t_2 = \gamma = 1$ and $t_3 = 0.2$.
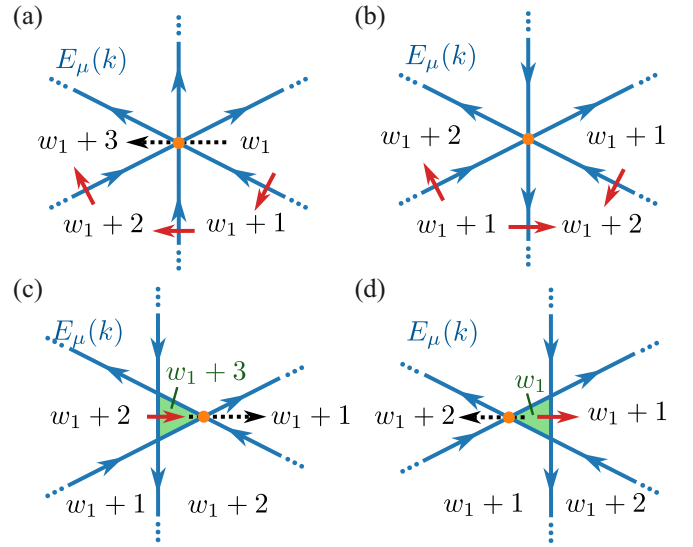

FIG. 4. (a) and (b) show the general two types of threefold self-intersection points. In the first type, the winding number can vary by up to 3 at the self-intersection point. In the second type, the change in winding number is limited to 1. However, small perturbations can split the second type into three double self-intersection points, generating a small loop with a winding number of w_1 in (c) or $w_1 + 3$ in (d). Both types of threefold self-intersection points lead to the condition $|\beta_{l+1}(E)| = |\beta_{l+2}(E)| = |\beta_{l+3}(E)| = 1$.

where $\mathcal{C}$ is the BZ curve. Using the same method as in the one-band case, it is obvious that self-intersection points in multiband systems also arise from the intersection between the aGBZ and BZ curves in the complex β plane.

As an illustrative example, we consider a non-Hermitian SSH model [68], which is shown in Fig. 3(a). The generalized Bloch Hamiltonian of this two-band model reads

$$h(\beta) = h_x(\beta)\sigma_x + h_y(\beta)\sigma_y;$$

$$h_x(\beta) = t_1 + \frac{t_2 + t_3 + \gamma}{2}\beta + \frac{t_2 + t_3 - \gamma}{2}\beta^{-1},$$

$$h_y(\beta) = i\frac{t_3 + \gamma - t_2}{2}\beta - i\frac{t_3 - \gamma - t_2}{2}\beta^{-1}, \qquad (15)$$

where $\sigma_{x,y,z}$ are the Pauli matrices. The absence of σ_z indicates that this model possesses sublattice (or chiral) symmetry $\sigma_z^{-1}h(\beta)\sigma_z = -h(\beta)$ [69], ensuring that the eigenvalues appear in pairs $(E, -E)$, as shown in Fig. 3(b). The characteristic equation of Hamiltonian (15) can be written as

$$h_x^2(\beta) + h_y^2(\beta) - E^2 = 0, \qquad (16)$$

which is a quartic equation for β. Upon arranging the four solutions in ascending order of magnitude, denoted as $|\beta_1| \leqslant |\beta_2| \leqslant |\beta_3| \leqslant |\beta_4|$, the aGBZ corresponds to the trajectory of β that satisfies the condition $|\beta_i| = |\beta_j|$. By numerically calculating the aGBZ in Fig. 3(c), we confirm that the self-intersection points of the PBC energy spectrum correspond to the intersections between the aGBZ and BZ curves.

V. THEORY OF MULTIPLE SELF-INTERSECTION POINTS

So far, we have primarily focused on the case of twofold self-intersection points, where the non-Hermitian energy

spectrum crosses the self-intersection point only twice. In this section, we extend our analysis to multiple self-intersection points with multiplicities greater than two.

We first consider the threefold self-intersection points in the PBC energy spectrum. These points, where the spectrum intersects itself thrice, connect six distinct regions and can be categorized into two types. Without loss of generality, the first type of threefold self-intersection points connects regions with a minimum winding number of $w_1 = l - M$ and a maximum winding number of $w_1 + 3$ [see Fig. 4(a)]. Similar to the analysis of double self-intersection points, we find that these points must satisfy $|\beta_{l+1}(E)| = |\beta_{l+2}(E)| = |\beta_{l+3}(E)| = 1$. The second type connects regions with a minimum winding number of $w_1 + 1$ ($l + 1 - M$) and a maximum winding number of $w_1 + 2$ [see Fig. 4(b)]. Introducing a small perturbation transforms these threefold self-intersection points into small loops. One case occurs when the loop has a winding number of w_1 [see Fig. 4(c)], resulting in the condition $|\beta_{l+1}(E)| = |\beta_{l+2}(E)| = 1$ for these self-intersection points. Another case arises when the loop has a winding number of $w_1 + 3$ [see Fig. 4(d)], leading to the requirement that $|\beta_{l+2}(E)| = |\beta_{l+3}(E)| = 1$. By combining these conditions, we find that for both types of threefold self-intersection points, $|\beta_{l+1}(E)| = |\beta_{l+2}(E)| = |\beta_{l+3}(E)| = 1$ always holds.

For general multiple self-intersection points with multiplicity n, we demonstrate that the n-fold self-intersection points of the spectrum correspond to n solutions of β on the BZ. The indices of these solutions are determined by the winding number in the vicinity of the n-fold self-intersection point, as well as the number of inward trajectories. In general, the neighborhood of an n-intersection point in the spectrum is divided into $2n$ regions, each possessing distinct winding
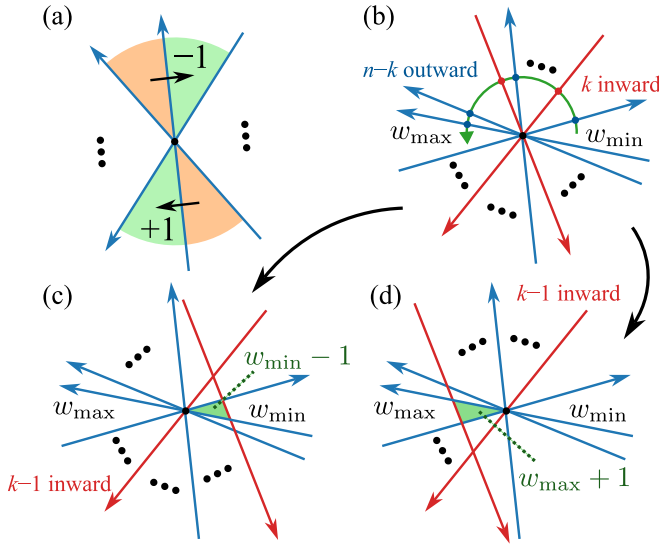
FIG. 5. General proof for the n-fold self-intersection point. (a) Relation of the sum of winding number in opposite regions. (b) Illustration of the n-fold self-intersection point, where the green arc starts from the region with minimal winding number, rotating anticlockwise to the region with maximal winding number. The red and blue arrowed lines are trajectories of the PBC spectrum intersecting with the green arc at the half pointing to and away from the n-fold self-intersection point, respectively. (c) and (d) Two perturbations of one inward trajectory, where the winding numbers in the green triangular regions are marked by green font, respectively.

numbers. As illustrated in Fig. 5(a), when two opposite regions (indicated by orange sectors) traverse along the same trajectory to adjacent opposite regions (depicted as green sectors), the increase in the winding number on one side is equal to the decrease on the other. Consequently, the sum of the winding numbers in opposite regions remains constant for a given n-fold self-intersection point. Therefore, the regions with the maximum winding number $w_{\min}$ and the minimum winding number $w_{\min}$ are positioned opposite to each other.

Consider the arc depicted in green in Fig. 5(b), which originates from the region with $w_{\min}$ and rotates counterclockwise towards the region with $w_{\max}$. Let us assume that the arc intersects $n - k$ trajectories extending outward from the n-fold intersection point (indicated by blue arrowed lines) and k trajectories directed inward (shown with red arrowed lines). When the arc crosses an outward (inward) trajectory, the winding number increases (decreases) by 1. Generally, the indices of the solutions for β can be expressed as $|\beta_{l_{\min}-k+1}| = |\beta_{l_{\min}-k+2}| = \cdots = |\beta_{l_{\max}+k}| = 1$, where $l_{\min} = M + w_{\min}$ and $l_{\max} = M + w_{\max}$. This result can be demonstrated using a recursion method. For the n-fold self-intersection point, if we pick one of the inward trajectories (represented by a red arrowed line), the multiplicity of the original self-intersection point is subsequently reduced by 1. For the perturbation shown in Fig. 5(c), the winding number of the green region is $w_{\min} - 1$, according to the relative position of the green region and the sector with $w_{\min}$. Conversely, for the perturbation shown in Fig. 5(d), the winding number of the green region is $w_{\max} + 1$ for the analogous reason. We assume that our observation holds for $(n-1)$-fold self-intersection

point. For the perturbation shown in Fig. 5(c), since the maximal and minimal winding numbers of the $(n - 1)$-fold self-intersection point are $w_{\max}$ and $w_{\min} - 1$, respectively, and the number of inward trajectories equals $k - 1$, the relation $|\beta_{l_{\min}-k+1}| = |\beta_{l_{\min}-k+2}| = \cdots = |\beta_{l_{\max}+k-1}| = 1$ also holds. Similarly, for the perturbation shown in Fig. 5(d), the relation $|\beta_{l_{\min}-k+2}| = |\beta_{l_{\min}-k+3}| = \cdots = |\beta_{l_{\max}+k}| = 1$ holds. By reducing the amount of perturbation to 0, both relationships will simultaneously hold for the n-fold self-intersection point, yielding $|\beta_{l_{\min}-k+1}| = |\beta_{l_{\min}-k+2}| = \cdots = |\beta_{l_{\max}+k}| = 1$. Since the cases of $n = 2$ and $n = 3$ have been substantiated in our previous discussions, this conclusion is validated for arbitrary n-fold self-intersection points through the recursion process. In Appendix C, we give a concrete method for constructing n-fold self-intersection points.

VI. SUMMARY AND DISCUSSION

In this study, we unveil the geometric origins of self-intersection points in one-dimensional PBC energy spectra. We rigorously demonstrate that the self-intersection points of one-band PBC energy spectra arise from the intersection between the aGBZ and the BZ, which is verified numerically in an extended Hatano-Nelson model. Furthermore, we extend our analysis to multiband cases, illustrated through a non-Hermitian SSH model. Moreover, we discuss the multiple self-intersection points, deriving the geometric conditions for general n-fold self-intersection points. We establish a one-to-multiple correspondence between non-Hermitian energy self-intersection points and the intersections between the aGBZ and the BZ. In general, for an n-fold self-intersection point E_0 of the PBC spectrum in the complex energy plane, the number of intersections, denoted as $\beta(E_0)$, between the aGBZ and the BZ in the complex β plane is equal to n.

When considering the case in which the dimension is greater than one, the definitions of the aGBZ and the self-intersection points of the spectrum appear ambiguous, as they involve multiple complex variables. Nonetheless, we can still apply our theory by analyzing one of the variables while holding the others constant. For instance, in the two-dimensional case, the generalized Bloch Hamiltonian for the one-band can be expressed as $h(\beta_x, \beta_y) = \sum_{m,n} c_{mn}(\beta_x)^m(\beta_y)^n$. The characteristic equation now takes the form $h(\beta_x, \beta_y) - E = 0$, which is challenging to solve. However, for each fixed β_x or β_y, we can solve the characteristic equation similarly to the one-dimensional case, determining the aGBZ and the self-intersection points of the PBC energy spectrum.

As shown in Fig. 2 and Fig. 3, when the winding numbers of the PBC spectra change sign, the corresponding self-intersection points are also located in the OBC spectra. This fact indicates that such self-intersection points serve as fixed points in the thermodynamic limit. In other words, as the system transitions from PBC to OBC by adjusting the boundary coupling [70,71], most PBC eigenstates transform into localized skin states, while the eigenstates associated with these self-intersection points remain extended. Additionally, the eigenstates corresponding to these self-intersection points exhibit scale-free properties in finite-size systems [41,72–75], thereby facilitating the experimental investigation of these special points.

ACKNOWLEDGMENTS

DATA AVILABILITY

The data that support the findings of this article are not publicly available. The data are available from the authors upon reasonable request.

APPENDIX A: CALCULATION OF aGBZ VIA THE RESULTANT METHOD

The calculation of aGBZ is the key to verify our results. In Appendix A, we give a brief introduction to the polynomial resultant theory and outline the detailed application of this useful method to obtain the aGBZ.

In mathematics, the resultant of two polynomials is used to identify the existence of a common factor, or equivalently, a common root. For two given polynomials $f(x) = a_n x^n + \cdots + a_0$ and $g(x) = b_m x^m + \cdots + b_0$, the resultant with respect to the variable x is a polynomial expression of their coefficients, defined as

$$\text{Res}_x[f(x), g(x)] = a_n^m b_m^n \prod_{i,j} (\xi_i - \eta_j), \qquad \text{(A1)}$$

where ξ_i and η_j are the root of $f(x)$ and $g(x)$, respectively, with $1 \leqslant i \leqslant n, 1 \leqslant j \leqslant m$. Apparently, the polynomials $f(x)$ and $g(x)$ share a common root if and only if their resultant $\text{Res}_x[f(x), g(x)]$ is zero. The resultant of $f(x)$ and $g(x)$ can be explicitly calculated using the Sylvester matrix, defined as follows:

$$\text{Syl}(f, g) = \begin{bmatrix} a_n & a_{n-1} & a_{n-2} & \cdots & 0 & 0 & 0 \\ 0 & a_n & a_{n-1} & \cdots & 0 & 0 & 0 \\ \vdots & \vdots & \vdots & & \vdots & \vdots & \vdots \\ 0 & 0 & 0 & \cdots & a_1 & a_0 & 0 \\ 0 & 0 & 0 & \cdots & a_2 & a_1 & a_0 \\ b_m & b_{m-1} & b_{m-2} & \cdots & 0 & 0 & 0 \\ 0 & b_m & b_{m-1} & \cdots & 0 & 0 & 0 \\ \vdots & \vdots & \vdots & & \vdots & \vdots & \vdots \\ 0 & 0 & 0 & \cdots & b_1 & b_0 & 0 \\ 0 & 0 & 0 & \cdots & b_2 & b_1 & b_0 \end{bmatrix}.$$

$$\text{(A2)}$$

It can be proved that the resultant defined by Eq. (A1) is just the determinant of their Sylvester matrix [76], namely

$$\text{Res}_x[f(x), g(x)] = \det \text{Syl}(f, g). \qquad \text{(A3)}$$

Using this relation, we can derive the analytical expression of the aGBZ curve on the complex β plane by eliminating the variables E and θ from the equation

$$f(\beta, E) = f(\beta e^{i\theta}, E) = 0, \theta \in \mathbb{R}. \qquad \text{(A4)}$$

To eliminate E, we can calculate the resultant of $f(\beta, E)$ and $f(\beta e^{i\theta}, E)$ with respect to E from Eq. (A3), and label this resultant as $G(\beta, \theta)$, namely

$$G(\beta, \theta) = \text{Res}_E[f(x), g(x)] = 0. \qquad \text{(A5)}$$

Since $G(\beta, \theta)$ is a complex algebraic function of β and $\beta e^{i\theta}$, the above equation can be separated into two independent real algebraic equations as

$$\text{Re}\, G(\beta, \theta) = 0, \text{Im}\, G(\beta, \theta) = 0. \qquad \text{(A6)}$$

Given that $\beta e^{i\theta} = \beta \cos \theta + i \beta \sin \theta$, the variable θ can not be directly eliminated using the resultant method. By substituting $\cos \theta = (1 - t^2)/(1 + t^2)$ and $\sin \theta = 2t/(1 + t^2)$, we can obtain the resultant of $\text{Re}\, G(\beta, t)$ and $\text{Im}\, G(\beta, t)$ with respect to t, leading to the expression for the aGBZ:

$$F_{\text{aGBZ}}(\text{Re}\,\beta, \text{Im}\,\beta) = \text{Res}_t[\text{Re}\, G(\beta, \theta), \text{Im}\, G(\beta, t)]. \quad \text{(A7)}$$

The above result of $F_{\text{aGBZ}}(\text{Re}\,\beta, \text{Im}\,\beta)$ is an algebraic polynomial of $\text{Re}\,\beta$ and $\text{Im}\,\beta$, representing a closed curve on the complex β plane. When evaluating $F_{\text{aGBZ}}(\text{Re}\,\beta, \text{Im}\,\beta)$, symbolic computing programs such as MATHEMATICA and MATLAB can efficiently automate the calculation of the resultant.

APPENDIX B: NUMBER OF ZEROS ENCLOSED BY SUB-aGBZ CURVES

In Appendix B, we show that each subcurve $\partial \mathcal{B}_{i,i+1}$ is the boundary of the open set that contains the i zeros of the characteristic equation. Consequently, $\partial \mathcal{B}_{i,i+1}$ is a closed curve that encircles these i zeros.

The single-band characteristic equation $h(\beta) - E = 0$ establishes a mapping from β to E, indicating that for each β, there exists a unique corresponding E. Conversely, for a given value of E, there are $m + n$ zeros in complex β plane, where m is the order of the pole. These zeros can be ordered by their magnitude: $|\beta_1(E)| \leqslant \cdots \leqslant |\beta_{m+n}(E)|$. As E sweep through the entire complex plane, we obtain a set of continuum areas $\mathcal{A}_1, \cdots, \mathcal{A}_{m+n}$. Here, the definition of open set $\mathcal{A}_i$ is given by

$$\mathcal{A}_i = \{\beta_i | \forall E \in \mathbb{C} : |\beta_{i-1}(E)| < |\beta_i(E)| < |\beta_{i+1}(E)|\}. \text{ (B1)}$$

If there is an intersection between $\mathcal{A}_i$ and $\mathcal{A}_j$, denoted as I_{ij}, then for any $\beta \in I_{ij}$, it follows that $\beta = \beta_i(E) = \beta_j(E')$ for $E \neq E'$. This implies that a single β corresponds to two distinct values, contradicting the injective nature of the function $E = h(\beta)$. Therefore, $\mathcal{A}_i$ and $\mathcal{A}_j$ do not intersect in single-band systems; geometrically, this means that $\mathcal{A}_i$ and $\mathcal{A}_j$ have no overlap.

The frontier of $\mathcal{A}_i$, denoted as $\partial \mathcal{A}_i$, is the set of points β such that every neighborhood of β contains both points in $\mathcal{A}_i$ and points not in $\mathcal{A}_i$. Mathematically, the frontier of $\mathcal{A}_i$ can be expressed as

$$\partial \mathcal{A}_i = \{\beta | \forall O \ni \beta : \mathcal{A}_i \cap O \neq 0, \mathcal{A}_i^C \cap O \neq 0\}, \qquad \text{(B2)}$$

where $\mathcal{A}_i^C = \mathbb{C} \backslash \mathcal{A}_i$ is the complementary set of $\mathcal{A}_i$. The boundary between $\mathcal{A}_i$ and $\mathcal{A}_j$ is defined as

$$\partial \mathcal{B}_{i,j} = \partial A_i \cap \partial A_j. \tag{B3}$$

Thus, we have

$$\partial \mathcal{B}_{i,j} = \{\beta_i, \beta_j \in \mathbb{C} | \forall E \in \mathbb{C} : |\beta_i(E)| = |\beta_j(E)|\} \tag{B4}$$

and the GBZ is $\partial \mathcal{B}_{m,m+1}$. Furthermore, we define the set $\mathcal{U}_{i,i+1}$ as the union of open sets $\mathcal{A}_1, \mathcal{A}_2, \cdots, \mathcal{A}_i$ and their boundaries $\partial \mathcal{B}_{r,s}$ ($1 \leqslant r, s \leqslant i$). The boundary of $\mathcal{U}_{i,i+1}$ is the subcurve $\partial \mathcal{B}_{i,i+1}$ of aGBZ. According to the definition of $\mathcal{U}_{i,i+1}$, its interior automatically contains the first i zeros for any $E \in \mathbb{C}$. As a result, the boundary $\partial \mathcal{B}_{i,i+1}$ forms a closed curve, enclosing the i zeros of the single-band characteristic equation $h(\beta) - E = 0$.

APPENDIX C: CONSTRUCTING THE n-FOLD SELF-INTERSECTION POINTS

In the main text, we derive the geometric conditions for general n-fold self-intersection points. Here, we present a straightforward and concrete method for constructing n-fold self-intersection points. Taking the one-band case as an example, we find that if the generalized Hamiltonian $h(\beta)$ can be expressed in the following form:

$$h(\beta) = (1 - e^{i\phi} \beta^n) q(\beta), \tag{C1}$$

where $q(\beta)$ is a holomorphic function of β such that $q(\beta) \neq 0$ when $|\beta| = 1$, and ϕ is a real number satisfying $0 \leqslant \phi < 2\pi$, then $h(\beta)$ exhibits n-fold self-intersection points at the origin of the complex energy plane. Specifically, the characteristic equation $h(\beta) - E = 0$ for $E = 0$ possesses n distinct solutions that satisfy $|\beta| = 1$. These solutions are given by:

$$\beta = e^{i\frac{2\pi m - \phi}{n}}, \quad m = 1, \cdots, n. \tag{C2}$$

For example, the generalized Hamiltonian in the Fig. 2(c) is

$$h_{\text{HN}}(\beta) = 0.5\beta^{-2} + 1.5\beta^{-1} + 0.5\beta + 1.5\beta^2$$
$$= (1 + \beta^3)(0.5\beta^{-2} + 1.5\beta^{-1}). \tag{C3}$$

In this case, we find $\phi = \pi$ and $q(\beta) = 0.5\beta^{-2} + 1.5\beta^{-1}$. The solutions for this threefold self-intersection point are $\beta = e^{i\frac{\pi}{3}}$, $e^{i\pi}$, and $e^{i\frac{5\pi}{3}}$, which is consistent with the numerical results shown in Fig. 2(f).

[1] R. El-Ganainy, K. G. Makris, M. Khajavikhan, Z. H. Musslimani, S. Rotter, and D. N. Christodoulides, Non-Hermitian physics and $\mathcal{PT}$ symmetry, Nature Phys. **14**, 11 (2018).

[2] L. Feng, R. El-Ganainy, and L. Ge, Non-Hermitian photonics based on parity–time symmetry, Nature Photon. **11**, 752 (2017).

[3] S. Longhi, Parity-time symmetry meets photonics: A new twist in non-Hermitian optics, Europhys. Lett. **120**, 64001 (2017).

[4] T. Ozawa, H. M. Price, A. Amo, N. Goldman, M. Hafezi, L. Lu, M. C. Rechtsman, D. Schuster, J. Simon, O. Zilberberg, and I. Carusotto, Topological photonics, Rev. Mod. Phys. **91**, 015006 (2019).

[5] I. Rotter, A non-Hermitian Hamilton operator and the physics of open quantum systems, J. Phys. A: Math. Theor. **42**, 153001 (2009).

[6] T. Yoshida, R. Peters, and N. Kawakami, Non-Hermitian perspective of the band structure in heavy-fermion systems, Phys. Rev. B **98**, 035141 (2018).

[7] H. Shen and L. Fu, Quantum oscillation from in-gap states and a non-Hermitian Landau level problem, Phys. Rev. Lett. **121**, 026403 (2018).

[8] K. Yamamoto, M. Nakagawa, K. Adachi, K. Takasan, M. Ueda, and N. Kawakami, Theory of non-Hermitian fermionic superfluidity with a complex-valued interaction, Phys. Rev. Lett. **123**, 123601 (2019).

[9] C. M. Bender, Making sense of non-Hermitian Hamiltonians, Rep. Prog. Phys. **70**, 947 (2007).

[10] H. Cao and J. Wiersig, Dielectric microcavities: Model systems for wave chaos and non-Hermitian physics, Rev. Mod. Phys. **87**, 61 (2015).

[11] V. V. Konotop, J. Yang, and D. A. Zezyulin, Nonlinear waves in $\mathcal{PT}$-symmetric systems, Rev. Mod. Phys. **88**, 035002 (2016).

[12] Y. Ashida, Z. Gong, and M. Ueda, Non-Hermitian physics, Adv. Phys. **69**, 249 (2020).

[13] E. J. Bergholtz, J. C. Budich, and F. K. Kunst, Exceptional topology of non-Hermitian systems, Rev. Mod. Phys. **93**, 015005 (2021).

[14] K. Ding, C. Fang, and G. Ma, Non-Hermitian topology and exceptional-point geometries, Nature Rev. Phys. **4**, 745 (2022).

[15] N. Okuma and M. Sato, Non-Hermitian topological phenomena: A review, Annu. Rev. Condens. Matter Phys. **14**, 83 (2023).

[16] K. Yang, Z. Li, J. L. K. König, L. Rødland, M. Stålhammar, and E. J. Bergholtz, Homotopy, symmetry, and non-Hermitian band topology, Rep. Prog. Phys. **87**, 078002 (2024).

[17] T. E. Lee, Anomalous edge state in a non-Hermitian lattice, Phys. Rev. Lett. **116**, 133903 (2016).

[18] S. Yao and Z. Wang, Edge states and topological invariants of non-Hermitian systems, Phys. Rev. Lett. **121**, 086803 (2018).

[19] S. Yao, F. Song, and Z. Wang, Non-Hermitian Chern bands, Phys. Rev. Lett. **121**, 136802 (2018).

[20] F. K. Kunst, E. Edvardsson, J. C. Budich, and E. J. Bergholtz, Biorthogonal Bulk-boundary correspondence in non-Hermitian systems, Phys. Rev. Lett. **121**, 026808 (2018).

[21] V. M. Martinez Alvarez, J. E. Barrios Vargas, and L. E. F. Foa Torres, Non-Hermitian robust edge states in one dimension: Anomalous localization and eigenspace condensation at exceptional points, Phys. Rev. B **97**, 121401(R) (2018).

[22] C. H. Lee and R. Thomale, Anatomy of skin modes and topology in non-Hermitian systems, Phys. Rev. B **99**, 201103(R) (2019).

[23] L. Xiao, T. Deng, K. Wang, G. Zhu, Z. Wang, W. Yi, and P. Xue, Non-Hermitian bulk–boundary correspondence in quantum dynamics, Nature Phys. **16**, 761 (2020).

[24] T. Helbig, T. Hofmann, S. Imhof, M. Abdelghany, T. Kiessling, L. Molenkamp, C. Lee, A. Szameit, M. Greiter, and R. Thomale, Generalized bulk–boundary correspondence in non-Hermitian topolectrical circuits, Nature Phys. **16**, 747 (2020).

[25] A. Ghatak, M. Brandenbourger, J. van Wezel, and C. Coulais, Observation of non-Hermitian topology and its bulk–edge correspondence in an active mechanical metamaterial, Proc. Natl. Acad. Sci. **117**, 29561 (2020).

[26] K. Yokomizo and S. Murakami, Non-Bloch band theory of non-Hermitian systems, Phys. Rev. Lett. **123**, 066404 (2019).

[27] S. Longhi, Probing non-Hermitian skin effect and non-Bloch phase transitions, Phys. Rev. Res. **1**, 023013 (2019).

[28] C. H. Lee, L. Li, and J. Gong, Hybrid higher-order skin-topological modes in nonreciprocal systems, Phys. Rev. Lett. **123**, 016805 (2019).

[29] K. Zhang, Z. Yang, and C. Fang, Correspondence between winding numbers and skin modes in non-Hermitian systems, Phys. Rev. Lett. **125**, 126402 (2020).

[30] Y. Yi and Z. Yang, Non-Hermitian skin modes induced by on-site dissipations and chiral tunneling effect, Phys. Rev. Lett. **125**, 186802 (2020).

[31] K. Kawabata, N. Okuma, and M. Sato, Non-Bloch band theory of non-Hermitian Hamiltonians in the symplectic class, Phys. Rev. B **101**, 195147 (2020).

[32] K. Kawabata, K. Shiozaki, and S. Ryu, Topological field theory of non-Hermitian systems, Phys. Rev. Lett. **126**, 216405 (2021).

[33] K. Zhang, Z. Yang, and C. Fang, Universal non-Hermitian skin effect in two and higher dimensions, Nature Commun. **13**, 2496 (2022).

[34] Y. Li, C. Liang, C. Wang, C. Lu, and Y.-C. Liu, Gain-loss-induced hybrid skin-topological effect, Phys. Rev. Lett. **128**, 223903 (2022).

[35] H.-Y. Wang, F. Song, and Z. Wang, Amoeba formulation of non-Bloch band theory in arbitrary dimensions, Phys. Rev. X **14**, 021011 (2024).

[36] H. Hu, Topological origin of non-Hermitian skin effect in higher dimensions and uniform spectra, Sci. Bull. **70**, 51 (2024).

[37] Y. Qi, J. Pi, Y. Wu, H. Lin, C. Zheng, and G.-L. Long, Extended imaginary gauge transformation in a general nonreciprocal lattice, Phys. Rev. B **110**, 075411 (2024).

[38] M. Zheng, Y. Qiao, Y. Wang, J. Cao, and S. Chen, Exact solution of the Bose-Hubbard model with unidirectional hopping, Phys. Rev. Lett. **132**, 086502 (2024).

[39] M. J. Colbrook, B. Roman, and A. C. Hansen, How to compute spectra with error control, Phys. Rev. Lett. **122**, 250201 (2019).

[40] Z. Yang, K. Zhang, C. Fang, and J. Hu, Non-Hermitian bulk-boundary correspondence and auxiliary generalized brillouin zone theory, Phys. Rev. Lett. **125**, 226402 (2020).

[41] L. Li, C. H. Lee, S. Mu, and J. Gong, Critical non-Hermitian skin effect, Nature Commun. **11**, 5491 (2020).

[42] C.-H. Liu, K. Zhang, Z. Yang, and S. Chen, Helical damping and dynamical critical skin effect in open quantum systems, Phys. Rev. Res. **2**, 043167 (2020).

[43] K. Yokomizo and S. Murakami, Scaling rule for the critical non-Hermitian skin effect, Phys. Rev. B **104**, 165117 (2021).

[44] F. Qin, Y. Ma, R. Shen, and C. H. Lee, Universal competitive spectral scaling from the critical non-Hermitian skin effect, Phys. Rev. B **107**, 155430 (2023).

[45] K. Kawabata, K. Shiozaki, M. Ueda, and M. Sato, Symmetry and topology in non-Hermitian physics, Phys. Rev. X **9**, 041015 (2019).

[46] N. Okuma, K. Kawabata, K. Shiozaki, and M. Sato, Topological origin of non-Hermitian skin effects, Phys. Rev. Lett. **124**, 086801 (2020).

[47] D. Nakamura, T. Bessho, and M. Sato, Bulk-boundary correspondence in point-gap topological phases, Phys. Rev. Lett. **132**, 136401 (2024).

[48] D. S. Borgnia, A. J. Kruchkov, and R.-J. Slager, Non-Hermitian boundary modes and topology, Phys. Rev. Lett. **124**, 056802 (2020).

[49] F. Song, S. Yao, and Z. Wang, Non-Hermitian topological invariants in real space, Phys. Rev. Lett. **123**, 246801 (2019).

[50] S. Ma, H. Lin, and J. Pi, Imaginary gap-closed points and dynamics in a class of dissipative systems, Phys. Rev. B **109**, 214311 (2024).

[51] Q.-B. Zeng, Non-Hermitian skin effect edge, Phys. Rev. B **106**, 235411 (2022).

[52] M. Berry, Physics of Nonhermitian degeneracies, Czech. J. Phys. **54**, 1039 (2004).

[53] C. Dembowski, B. Dietz, H.-D. Gräf, H. L. Harney, A. Heine, W. D. Heiss, and A. Richter, Encircling an exceptional point, Phys. Rev. E **69**, 056216 (2004).

[54] D. Leykam, K. Y. Bliokh, C. Huang, Y. D. Chong, and F. Nori, Edge modes, degeneracies, and topological numbers in non-Hermitian systems, Phys. Rev. Lett. **118**, 040401 (2017).

[55] Y. Xiong, Why does bulk boundary correspondence fail in some non-Hermitian topological models, J. Phys. Commun. **2**, 035043 (2018).

[56] S.-X. Wang and Z. Yan, General theory for infernal points in non-Hermitian systems, Phys. Rev. B **110**, L201104 (2024).

[57] C. H. Lee, Exceptional bound states and negative entanglement entropy, Phys. Rev. Lett. **128**, 010402 (2022).

[58] F. Qin, R. Shen, and C. H. Lee, Nonlinear Hall effects with an exceptional ring, arXiv:2411.06509.

[59] L. V. Ahlfors, *Complex Analysis* (McGraw-Hill, New York, 1979), Vol. 3.

[60] N. Hatano and D. R. Nelson, Localization transitions in non-Hermitian quantum mechanics, Phys. Rev. Lett. **77**, 570 (1996).

[61] N. Hatano and D. R. Nelson, Vortex pinning and non-Hermitian quantum mechanics, Phys. Rev. B **56**, 8651 (1997).

[62] C. M. Bender and S. Boettcher, Real spectra in non-Hermitian Hamiltonians having *PT* symmetry, Phys. Rev. Lett. **80**, 5243 (1998).

[63] C. M. Bender, M. V. Berry, and A. Mandilara, Generalized PT symmetry and real spectra, J. Phys. A **35**, L467 (2002).

[64] S. Longhi, Non-Bloch $\mathcal{PT}$ symmetry breaking in non-Hermitian photonic quantum walks, Opt. Lett. **44**, 5804 (2019).

[65] L. Xiao, T. Deng, K. Wang, Z. Wang, W. Yi, and P. Xue, Observation of non-Bloch parity-time symmetry and exceptional points, Phys. Rev. Lett. **126**, 230402 (2021).

[66] Z. Lei, C. H. Lee, and L. Li, Activating non-Hermitian skin modes by parity-time symmetry breaking, Commun. Phys. **7**, 100 (2024).

[67] Y.-M. Hu, H.-Y. Wang, Z. Wang, and F. Song, Geometric origin of non-Bloch $\mathcal{PT}$ symmetry breaking, Phys. Rev. Lett. **132**, 050402 (2024).

[68] W. P. Su, J. R. Schrieffer, and A. J. Heeger, Soliton excitations in polyacetylene, Phys. Rev. B **22**, 2099 (1980).

[69] S. Ryu, A. P. Schnyder, A. Furusaki, and A. W. W. Ludwig, Topological insulators and superconductors: Tenfold way and dimensional hierarchy, New J. Phys. **12**, 065010 (2010).

[70] C.-X. Guo, C.-H. Liu, X.-M. Zhao, Y. Liu, and S. Chen, Exact solution of non-Hermitian systems with generalized boundary

conditions: Size-dependent boundary effect and fragility of the skin effect, Phys. Rev. Lett. **127**, 116801 (2021).

[71] M. Parto, C. Leefmans, J. Williams, R. M. Gray, and A. Marandi, Enhanced sensitivity via non-Hermitian topology, Light Sci. Appl. **14**, 6 (2025).

[72] L. Li, C. H. Lee, and J. Gong, Impurity induced scale-free localization, Commun. Phys. **4**, 42 (2021).

[73] B. Li, H.-R. Wang, F. Song, and Z. Wang, Scale-free localization and $\mathcal{PT}$ symmetry breaking from local non-Hermiticity, Phys. Rev. B **108**, L161409 (2023).

[74] C.-X. Guo, X. Wang, H. Hu, and S. Chen, Accumulation of scale-free localized states induced by local non-Hermiticity, Phys. Rev. B **107**, 134121 (2023).

[75] W. Li, Z. Sun, Z. Yang, and F. Li, Universal scalefree non-Hermitian skin effect near the Bloch point, Phys. Rev. B **109**, 035119 (2024).

[76] S. Lang, *Algebra* (Springer, Berlin, 2012), Vol. 211.